

Date of publication xxxx 00, 0000, date of current version xxxx 00, 0000.

Digital Object Identifier 10.1109/ACCESS.2023.Doi Number

Modeling and Analysis of Quasi-3D Equivalent Magnetic Network of Direct-drive Inner Boost Permanent Magnet Motor

JIACHENG WU¹, SHUAI WANG², YAN HU¹, BINGYI ZHANG¹, and XUEFENG XU¹

¹School of Electrical Engineering, Shenyang University of Technology, Shenyang 110870, China

²National Engineering Research Center for Rare-earth Permanent Magnet Machines, Shenyang University of Technology, Shenyang 110870, China

Corresponding author: Shuai Wang (e-mail: wangshuai@sut.edu.cn).

ABSTRACT To address the problems of low space utilization and weak overload capacity of traditional dual-stator permanent magnet motors with equal-length cores, a kind of inner boost permanent magnet motor (IBPMM) with unequal-length cores is proposed. First, the topological structure and inner stator start-stop control method of the IBPMM are introduced. Then, aiming at the problem that finite element model (FEM) is difficult to analyze the variation law of the outer stator torque when the rotor yoke is saturated caused by the high inner stator current, a new quasi-3D equivalent magnetic network (EMN) model with invariable air-gap permeance and accounting for saturation and flux leakage is proposed by using superposition method. The model is used to analyze air-gap flux density, flux linkage and no-load EMF of the IBPMM under different working conditions, and further separates the inner stator torque and outer stator torque, so as to analyze the change of the outer stator torque under different high-density inner stator currents. According to the quasi-3D EMN results, the proposed IBPMM has 3 times short-term overload capacity, and the outer stator torque decreases by only approximately 0.5% at the maximum inner boost current. Finally, the performance of the proposed IBPMM and the accuracy of the quasi-3D EMN are verified by 3D FEM and prototype experiments.

INDEX TERMS dual-stator permanent magnet motor, equivalent magnetic network, inner boost permanent magnet motor, short-term high overload, unequal-length cores.

I. INTRODUCTION

Owing to its high torque density and reliability, permanent magnet synchronous motor (PMSM) is often used in low-speed and high-torque direct-drive systems, such as coal mining, ship propulsion, wind power generation and other occasions [1-5]. With the gradual maturity of the PMSM theory, dual-stator permanent magnet motors (DSPMMs) with various topologies have been proposed to obtain higher torque density. Meanwhile, rapid and accurate analysis methods for PMSM with complex structures have been widely concerned.

Scholars have carried out a lot of in-depth research on DSPMM with high torque density, and obtained many valuable conclusions. In [6], a DSPMM with a permanent magnet and reluctance hybrid rotor was proposed, in which the inner reluctance rotor can improve the stability of the motor, but leads to a low power density of the inner stator, and its MTPA control mode was further studied in [7].

Literature [8] proposed a low-speed and high-torque DSPMM structure, and compared it with single-stator PMSM under the condition of equal-length cores, the results showed that the torque density of DSPMM is 1.54 and 1.52 times that of spoke and surface mounted single-stator PMSM, respectively, however, the end space of outer stator core is wasted due to the structure of equal-length cores. Literature [9] proposed a dual-stator spoke array vernier permanent magnet motor with high power factor and high torque density, and combined analytical method with the finite element method (FEM) to make the design process simpler and the results more reliable. Literature [10] proposed a DSPMM with radially magnetized cylindrical permanent magnet, compared with the traditional pole-arc PMSM, the proposed motor has lower cogging torque, however, the structural strength of the rotor cannot meet the high-torque load.

Much attention has also been paid to magnetic field analysis methods for complex topological motors. The lumped magnetic circuit model can quickly analyze the parameters of the motor, however, it cannot obtain high-precision results because of its rough regional division, moreover, it also cannot obtain parameters such as the air-gap flux density waveform [11]. 3D FEM has higher accuracy in motor parameter analysis, but it is difficult to separate the torque of DSPMSM, and for large-volume motors, a large number of mesh elements are required to obtain satisfactory accuracy, resulting in a long calculation time, which limits its practicability in the initial design and optimization process of such motors [12]. EMN model can accurately separate the electromagnetic torque of the DSPMSM, at the same time, it has a moderate amount of computation and high accuracy, therefore, it can be an alternative to the lumped parameter model and FEM [13-16]. To solve the problem of low calculation accuracy of traditional EMN in the complex area of flux distribution, pentagonal and hexagonal mesh elements are often used to model the area near the air-gap. Although this modeling method can improve the calculation accuracy of complex area of flux distribution, these two mesh elements have strict requirements on the shape and size of the element, so the universality is poor [17,18]. The hybrid cruciform mesh modeling method avoids the calculation of dynamic permeance, however, there are complex mesh elements containing two kinds of materials in the model, and the approximate solution of the element permeance will affect the accuracy in high saturation regions[19]. Literature [20] proposed a 3D EMN to model and solve the hub motor with hybrid excitation, and the solution accuracy is in good agreement with the 3D FEM results, however, this model is more complicated when dealing with the relative motion of the stator and rotor.

Although there are many studies on DSPMM, these studies are based on equal-length cores structure, which results in underutilization of the outer stator end space, it is worth noting that this problem is more obvious for low-speed direct-drive motor. Meanwhile, both the inner and outer stators are designed according to the long-term duty type, which limits the short-term overload capacity of the motor. To solve the above problems, an IBPMM with unequal-length cores is proposed in this paper. Firstly, the topological structure and working principle of the motor are introduced. Then, aiming at the problem that FEM is difficult to separate the inner and outer stator torque and has low solving efficiency, while the traditional EMN has difficulty in modeling the dynamic air-gap mesh and there are large errors in high-saturation regions, a quasi-3D EMN with invariable air-gap permeance and accounting for saturation and flux leakage is established by using superposition method to analyze the electromagnetic performance of the IBPMM under different working conditions and the influence of high inner stator current

density on outer stator torque, meanwhile the solving efficiency of the IBPMM is improved. Finally, the results of quasi-3D EMN are compared with the results of 3D FEM and the experimental data of the prototype, which verifies the performance of the proposed IBPMM, meanwhile, the rapidity and accuracy of the quasi-3D EMN model are also verified.

II. STRUCTURE AND WORKING PRINCIPLE OF IBPMM

A. STRUCTURE OF IBPMM

The basic structure of the IBPMM is shown in Fig. 1. In order to ensure mechanical strength, the rotor adopts a closed structure, the rotor yoke is supported by the front and back end-plates, and the entire rotor is fixed on the support shaft by two bearings. The output shaft is connected to the front end-plate of the rotor and is connected to the load through the bearing in the front cover of the housing. The inner and outer surfaces of the rotor yoke are equipped with surface-mounted PMs.

Compared with the traditional DSPMM with equal-length cores shown in Fig. 2, in order to make full use of the inner space of the motor to obtain a higher torque density, two stator cores of different lengths are arranged on the inner and outer sides of the rotor in the proposed IBPMM, and the axial length of the outer stator core is greater than that of the inner stator core. The inner stator is fixed by a support shaft with water path, and the outer stator is fixed to the housing with water path. In order to weaken the magnetic coupling between the inner and outer stators to make the control more stable, a parallel magnetic circuit structure is adopted between the inner and outer stators. In order to prevent the displacement of the PMs along the circumference, non-magnetized stainless steel press plates as shown in the Fig. 3. are used to press the PMs on rotor yoke.

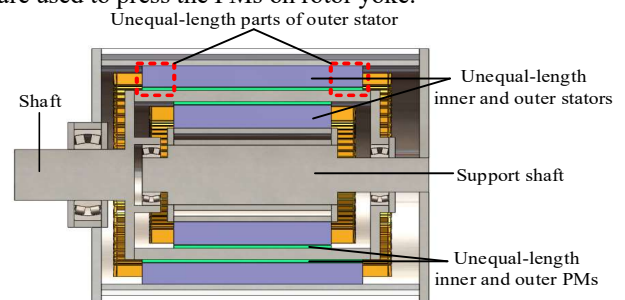


FIGURE 1. The structure of proposed IBPMM with unequal-length cores

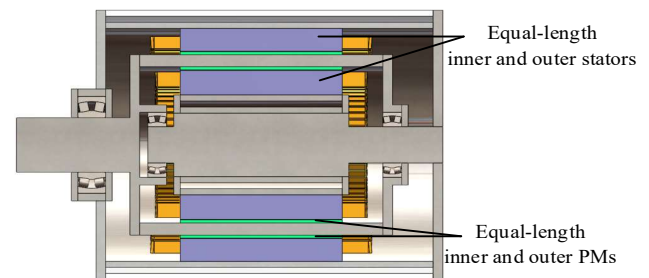


FIGURE 2. The structure of traditional DSPMM with equal-length cores

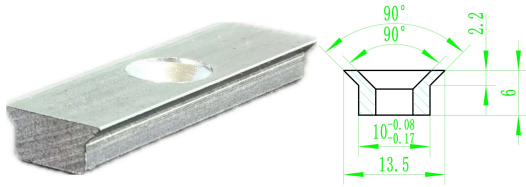


FIGURE 3. Stainless steel press plate

B. WORKING PRINCIPLE OF IBPMM

Due to the parallel magnetic circuit is used between the inner and outer stators of the IBPMM, they can be designed separately according to the operating characteristics. In order to meet the efficiency requirements of the S1 duty type, the outer stator is designed as a high-efficiency low-speed high-torque motor. While, in order to meet the torque density requirements of short-term high overload, the inner stator is designed to be a torque motor of short-term boost operation, which allows a large current in a short time to produce a high output torque. The inner stator cannot run for a long time due to its large current density, so when the IBPMM is in light-load operation, only the outer stator runs alone. When the load is large, the inner stator is started, so that the inner and outer stators generate torque to drive the load simultaneously. The two stators are driven by separate inverters. The control principle of the IBPMM is illustrated in Fig. 4. The torque distributor is used to control the operating state of the inner stator inverter and provide a reference torque for the inner and outer stators.

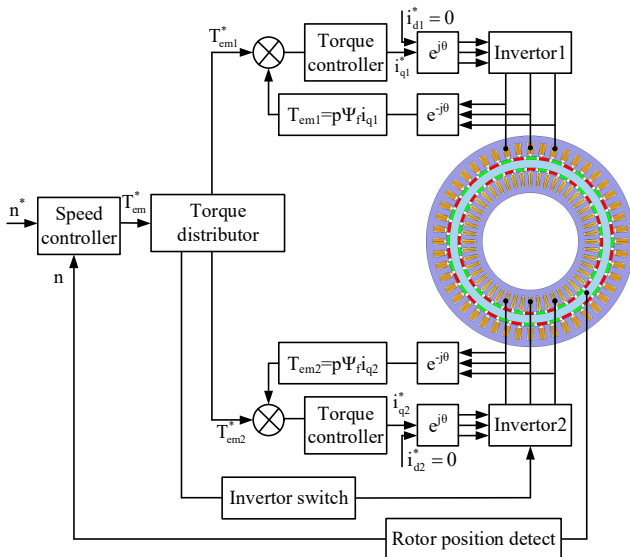


FIGURE 4. Control schematic diagram of IBPMM

The operating logic of the torque distributor is illustrated in Fig. 5. To make full use of the overload capacity of the outer stator, T_{on} is set as the maximum overload torque of the outer stator T_{outmax} . When the reference torque $T_{cm}^* > T_{on}$, the inverter2 of the inner motor is started, and a constant reference torque T_{em1IB} is provided to the outer stator. To

reduce the start-stop frequency of the inner stator near the starting point, both T_{em1IB} and T_{off} are set as $0.95T_{outmax}$. When $T_{cm}^* < T_{off}$, inverter2 of the inner stator is turned off, and only the outer stator works alone.

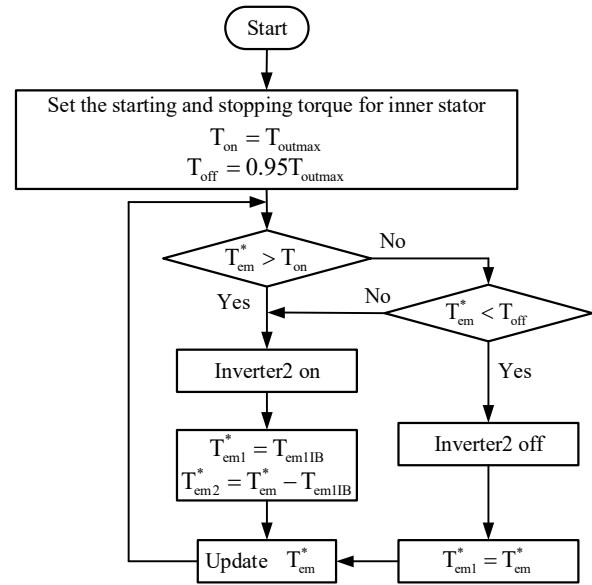


FIGURE 5. Torque distributor operation logic

The main parameters of the IBPMM prototype are shown in Table 1.

TABLE I
Main Parameters of the prototype

Parameter	Unit	Value
Rated power of outer stator	kW	90
Overload multiples of outer stator	-	1.8
Maximum power of inner stator	kW	120
Maximum overload multiples	-	3
Rated speed	r/min	60
Rated frequency	Hz	20
Rated Voltage	V	1140
Number of slots	-	48
Number of poles	-	40
Inner/outer diameter of inner stator	mm	330/492.4
Inner/outer diameter of outer stator	mm	620/770
Inner/outer stator core length	mm	500/650
PM remanent flux density B_r 20°C	T	1.36

III. QUASI-3D EMN MODELING FOR IBPMM

A. BASIC MESH ELEMENTS OF EMN

The EMN model of motor often involves three commonly used cruciform basic mesh elements: rectangle, trapezoid and sector. Their shape and permeance calculation formulas are shown in Fig. 6.

u_0 is the magnetic potential of the middle node of the element, and u_1-u_4 is the magnetic potential of the boundary. They are connected to the surrounding elements. The corresponding branch equation can be expressed as (1):

$$G_b(u_0 - u_b \pm F) = \Phi_b \quad (b=1,2,3,4) \quad (1)$$

where, G_b is the equivalent permeance in the branch; F is the magnetomotive force source in the branch.

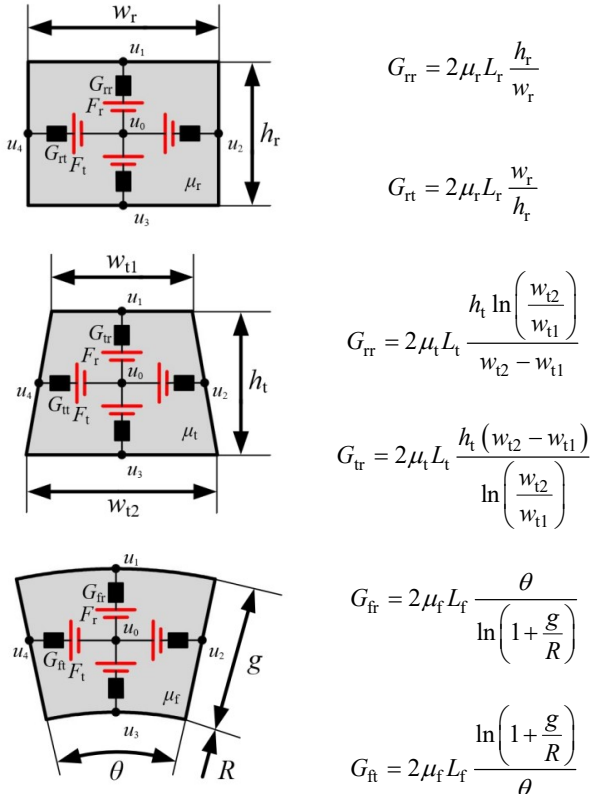


FIGURE 6. The basic mesh elements

B. MODELING OF STATOR EMN

The cross-sections of the inner and outer stator teeth and yokes remain unchanged, and the flux is evenly distributed. To reduce the number of nodes and computation, these two parts are represented by lumped parameters, and the flux leakage in the slot is also represented by lumped parameters. The stator tooth-tips have a high degree of saturation and complex distribution of flux, and the slot opening parts have a non-negligible flux leakage, so the cruciform mesh elements are used to model the tooth-tips and the slot opening parts. The EMN model of the stator part is shown in Fig. 7.

The stator teeth, stator tips and slot opening regions are modeled using rectangular permeance, the stator yoke is modeled using sectorial permeance, and the stator slot leakage is modeled using trapezoidal permeance. Solid element represents the nonlinear permeability element of ferromagnetic materials, and the hollow element represents the linear permeability element of the air material.

Since the IBPMM model adopts concentrated winding, the expression of the magnetomotive force F_{coil} generated by the coil is shown in (2), and the direction of the magnetomotive force is determined by the left-hand spiral rule.

$$F_{coil} = \oint H dl = NI \quad (2)$$

where, H is the magnetic field intensity; l is the loop circumference; N is the number of coil turns; I is the current in each coil.

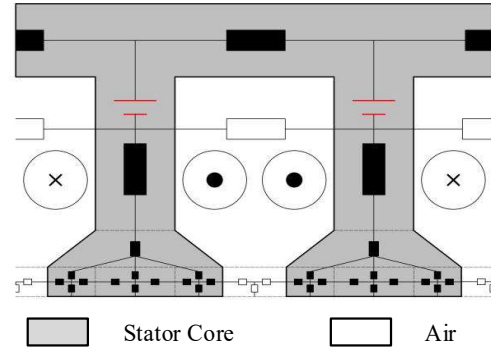


FIGURE 7. The stator EMN model

C. MODELING OF ROTOR EMN

The distribution of the flux inside the PM is regular, however, to consider the leakage flux between the adjacent PMs, the PMs and the air parts between them are modeled with cruciform mesh elements. The IBPMM adopts a parallel magnetic circuit, resulting in two parallel magnetic field lines in the rotor yoke, thus, double layers of cruciform mesh are used to model the rotor yoke. The PM, air region between PMs and the rotor yoke are all modeled by sectorial permeance. The EMN model of the rotor is shown in Fig. 8.

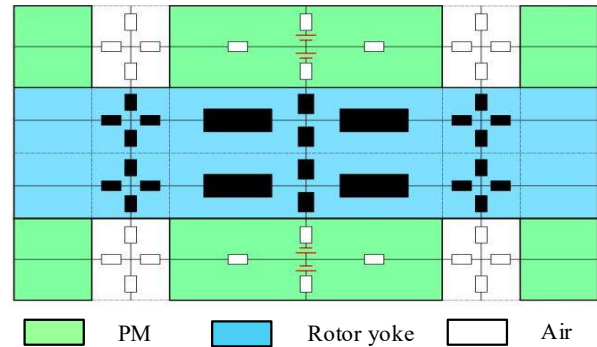


FIGURE 8. The rotor EMN model

Each magnetomotive force source inside PM can be expressed as (3)[21]:

$$F_{PM} = \frac{B_r h_{PM}}{2\mu_{PM}\mu_0} \quad (3)$$

where, B_r is remanent flux density; h_{PM} is the thickness in the magnetizing direction; μ_0 is the vacuum permeability; μ_{PM} is the relative permeability of the PM.

D. MODELING OF AIR-GAP EMN

The modeling of air-gap region is very important for EMN model, because it affects not only the solving accuracy, but also the relative motion simulation between stator and rotor. Although the equivalent magnetic circuit method can save calculation time by generating fewer mesh elements, the air-gap magnetic circuit element is a unidirectional equivalent

flux tube, therefore, it is difficult to accurately simulate the region with irregular geometry and complex flux distribution, especially in the region around the air-gap, and the tangential flux cannot be considered. In addition, using the equivalent magnetic circuit method to model the air-gap region requires adjusting the permeance according to the flux distribution, which will cause the corresponding permeance to change with the change of the flux path, which complicates the relative motion simulation. In order to solve the above problems, a double layers cruciform mesh is used to model the air-gap region, and the circumferential width of each mesh element in the air-gap region is consistent with the rotation step angle. A smaller rotation step angle and more radial layers will lead to more accurate calculation results, however, an excessive number of radial layers has a limited effect on the accuracy of the calculation results, and more air-gap meshes will be generated, resulting in longer calculation time [22]. Therefore, this paper divides the air gap mesh into two layers along the radial direction, and the layer near the stator forms a fixed connection with the stator tooth-tips mesh elements, and the layer near the rotor forms a fixed connection with the PMs and moves along with the rotor. Every mesh element divided in this manner contains only one material, and does not produce a complex mesh containing two materials, which simplifies the calculation of element permeance and ensures the calculation accuracy. The EMN model of the air-gap region is shown in Fig. 9.

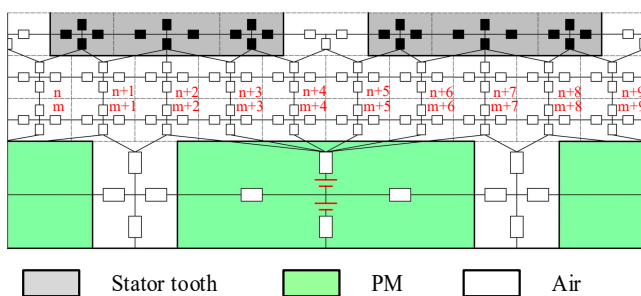


FIGURE 9. The air-gap EMN model

When simulating rotor rotation, suppose that the element n in the first layer air-gap is connected with the element m in the second layer air-gap at a certain moment. Then the element n in the first layer air-gap is connected with the element $m+1$ in the second layer air-gap at the next moment, and so on for subsequent movements. In this way, the rotation of the rotor can be simulated only by changing the connection between the two layers of air-gap elements, thus avoiding the re-modelling of the air-gap at different rotor positions and the composite mesh elements containing multiple materials. It should be noted that for the readability of the figure, the circumferential angle of each air-gap mesh element in Fig. 9. is 1.5° , however, to achieve sufficient calculational accuracy, the circumferential angle of each air-gap mesh element is set to 0.25° during the actual modeling.

E. QUASI-3D EMN MODEL OF IBPMM

The cross-section of the IBPMM is different along the axis, but its axial flux density is very small, in order to quickly analyze the IBPMM, the axial flux density is ignored. In this paper, the IBPMM is segmented into two parts along the axis, the single-stator part and dual-stator part, as shown in Fig. 10.

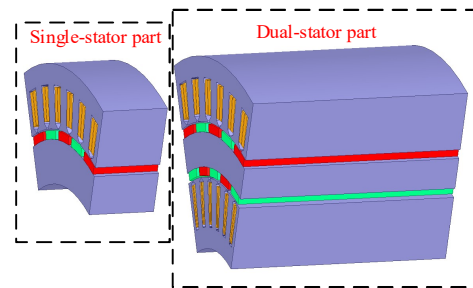


FIGURE 10. The segmentation diagram of IBPMM

2D EMN models of these two parts are established respectively, and then the two 2D models are constructed a quasi-3D EMN model by the superposition method, so as to analyze the performance of the IBPMM. In addition, due to the large axial length and thickness of the PMs of low-speed and high-torque PMSM, the leakage flux ratio at the end is small, therefore, the influence of leakage flux at the end is ignored in the proposed model.

The 2D EMN model of each part includes the stator, rotor and air-gap parts mentioned above, as shown in Fig. 11, where Fig. 11(a). is the EMN model of the dual-stator part in the middle of the IBPMM, and Fig. 11(b). is the EMN model of the part with only the outer stator on one side of the IBPMM.

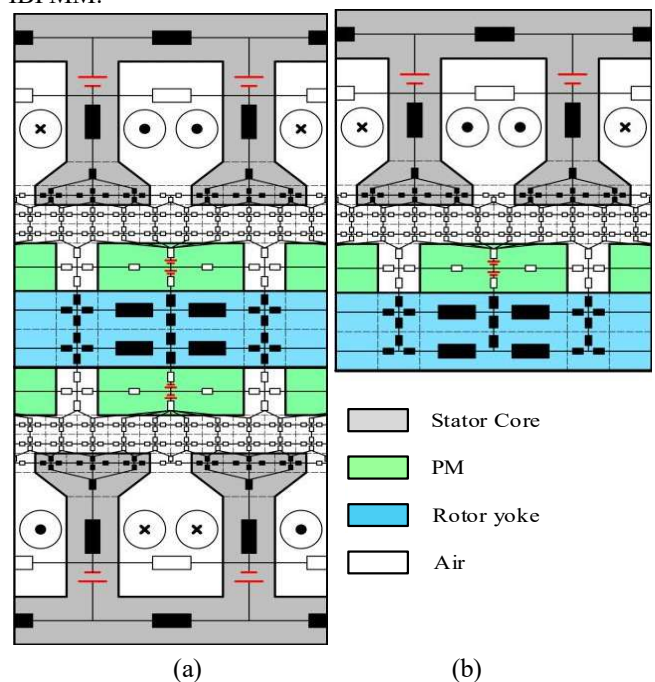


FIGURE 11. Segmentation EMN model of IBPMM (a) Dual-stator section (b) Single-stator section

F. NONLINEAR EMN MODEL SOLVING

Once the EMN model proposed in this paper is established, the number of nodes and branches remained unchanged. The basic equations for solving the EMN model by using the nodal voltage method can be expressed as (4)-(7):

$$\Phi = \mathbf{F}\mathbf{G} \quad (4)$$

$$\Phi = [\Phi(1) \cdots \Phi(n)]^T \quad (5)$$

$$\mathbf{F} = [F(1) \cdots F(n)]^T \quad (6)$$

$$\mathbf{G} = \begin{bmatrix} G(1,1) & G(1,2) & \cdots & G(1,n) \\ G(2,1) & G(2,2) & \cdots & G(2,n) \\ \vdots & \vdots & & \vdots \\ G(n,1) & G(n,2) & \cdots & G(n,n) \end{bmatrix} \quad (7)$$

where, n is the number of nodes of the EMN model; each element of $\Phi(i)$ represents the flux through node i ; each element $F(i)$ represents the magnetomotive force of node i ; each element $G(i, j)$ is the permeance between node i and node j , and $G(i, i)$ is the sum of all the permeances connected to node i .

The permeance and permeability in the model are satisfied (8).

$$\begin{cases} G(i, i) \geq 0, G(i, j) \leq 0 & i \neq j \\ G(i, i) = \sum_{j=1, j \neq i}^n -G(i, j) \\ G(i, j) = G(j, i) & i \neq j \\ \mu(i, j) = \mu(j, i) & i \neq j \end{cases} \quad (8)$$

The permeance matrix is a sparse matrix, but due to the large number of nodes of the EMN model, in order to speed up matrix solving, the overrelaxation iterative algorithm (9) is used to solve the matrix.

$$F_i^{(k+1)} = F_i^{(k)} + \frac{\omega}{G(i, i)} [\Phi(i) - \sum_{j=1}^{i-1} G(i, j)F_j^{(k+1)} - \sum_{j=i}^n G(i, j)F_j^{(k)}] \quad (9)$$

where, ω is the relaxation factor, and $0 < \omega < 2$, $\omega = 1.3$ is finally determined as the best by step search method with step size of 0.1.

When the node satisfies (10), the iteration process ends.

$$|F^{(k)} - F^{(k-1)}| < 10^{-5} \quad (10)$$

After solving the magnetomotive force of each node according to the above formulas, the flux density B between node i and node j can be solved using (11).

$$B = \frac{|F(i) - F(j) - F_s| G(i, j)}{S_{ij}} \quad (11)$$

where, $F(i)$ and $F(j)$ are the magnetomotive forces at node i and j , respectively. F_s is the magnetomotive force generated between node i and j by winding or PM. S_{ij} is the cross sectional area of the permeance element perpendicular to the direction of the flux between nodes i and j .

For nonlinear materials such as iron core and rotor yoke, after obtaining flux density B , the relative permeability is obtained by interpolating B - H characteristic curve of the material. To consider the effect of saturation, the permeability of these meshes must be calculated iteratively, and (12) is adopted to accelerate the iteration speed.

$$\mu_{\text{up}} = \mu_k^{p_1} \mu_{k-1}^{p_2} \quad (12)$$

where, $p_1=0.95$, $p_2=0.05$; μ_{up} is the updated permeability of the nonlinear element.

The iteration is terminated when the errors of the flux density of all nonlinear elements are less than 0.001 after iterations, that is:

$$\max |B^{(k)}(i, j) - B^{(k+1)}(i, j)| < 0.001 \quad (13)$$

The overall solving process of nonlinear EMN model is shown in Fig. 12.

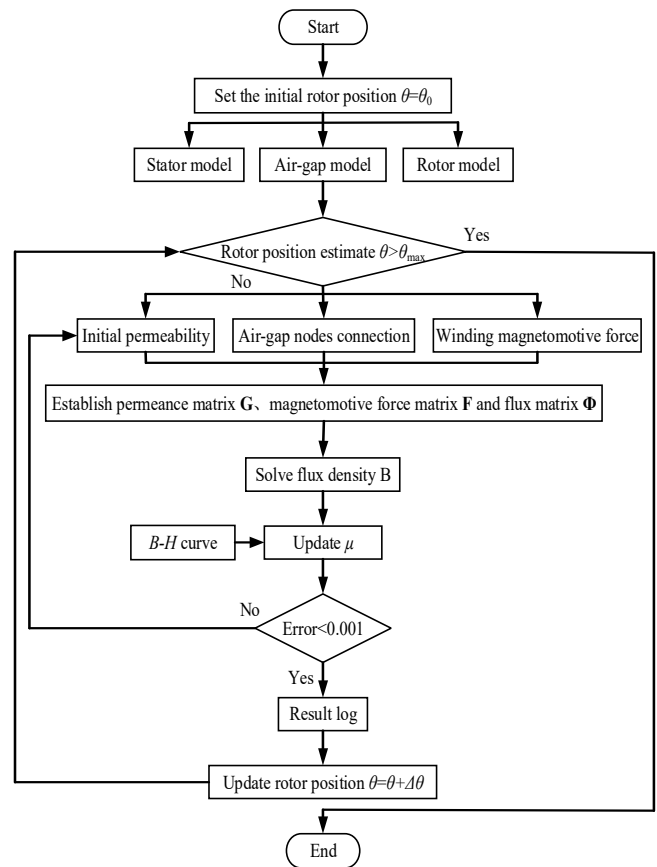


FIGURE 12. Solving process of nonlinear EMN model

IV. QUASI-3D EMN MODELING FOR IBPMM

To verify the correctness of the torque output capability of the proposed IBPMM and the analytical results of the quasi-3D EMN model, the results of the quasi-3D EMN are compared with 3D FEM results, including air-gap flux density, winding flux linkage, EMF and output torque under different excitations. The meshing result of the 3D FEM model is shown in Fig. 13.

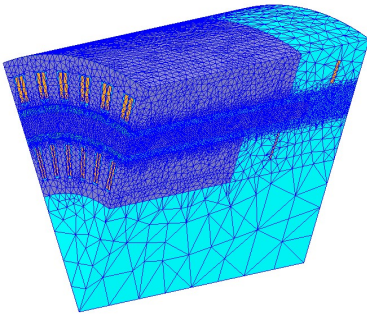


FIGURE 13. 3D FEM meshing result of IBPMM

A. PERFORMANCE COMPARISON UNDER NO-LOAD OPERATION

Since the quasi-3D EMN model is superimposed by two 2D EMN models, in order to verify its accuracy, the no-load radial air-gap flux density calculation results of the two EMN models are compared with the results obtained in the middle of each section of the 3D FEM model respectively, viz. at the axial 125mm and 287.5mm. The comparison results are shown in Fig. 14.

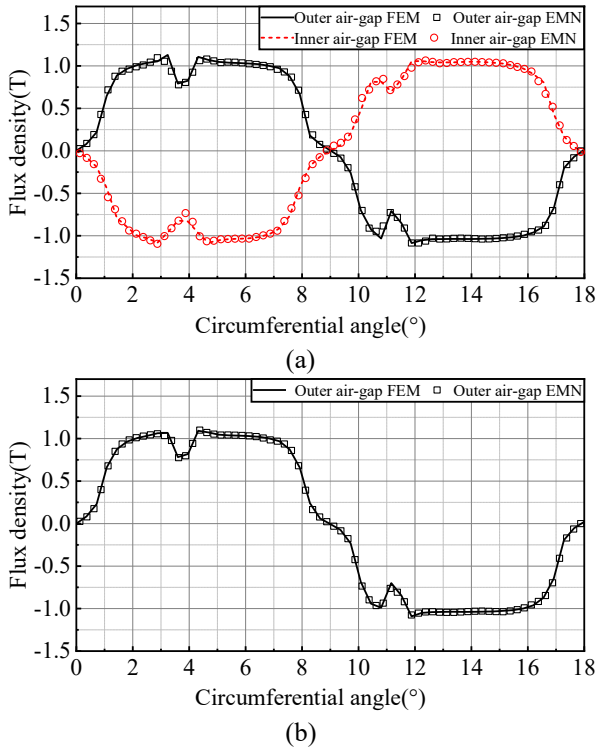


FIGURE 14. Comparison of no-load air-gap radial flux density (a) Dual-stator part (b) Single-stator part

Fig. 14(a) and 14(b) show the radial flux density comparison results of the inner and outer air-gaps in the dual-stator part and the radial flux density comparison results of the the air-gap only in the outer stator part. Because the proposed EMN model uses a detailed air-gap meshing and the saturation degree of the cores is low under no-load operation, the two calculation results have a good agreement,

and there are some errors only in the slot opening regions, which are caused by the EMN model's less precise meshing of the flux leakage path near the slot opening than the FEM. (14) is used to compare the error between EMN and FEM results [23].

$$\delta = \frac{\sum_{i=1}^n \left| \frac{B_{FEMi} - B_{EMNi}}{B_{FEMi}} \right|}{n} \times 100\% \quad (14)$$

where, δ is the calculation error; B_{EMNi} is the flux density of the air-gap at the node i of the EMN model; B_{FEMi} is the FEM flux density result at the same position as the node i of the EMN model; n is the total number of air-gap elements in the EMN model.

Through error analysis, the errors of the inner and outer air-gap flux density in the dual-stator part are 2.2% and 2.0% respectively, and the error of the single stator part is 1.9%.

The calculation formulas for the phase flux linkage and EMF are shown in (15) - (17) :

$$\psi_j = \sum_{i=1}^n \frac{N\Phi_i}{a} \quad (15)$$

$$E_j = -\frac{d\psi_j}{dt} \quad (16)$$

where, $j=U, V, W$ represents the three phases U, V, W; n is the number of teeth surrounded by each phase winding; N is the number of coil turns; a is the number of parallel branches per phase.

Since the EMN model of the outer stator winding is composed of two parts, its flux linkage is obtained by superposition of the two EMN results:

$$\Psi_{jout} = \Psi_{jout1} + \Psi_{jout2} \quad (17)$$

where, Ψ_{jout} is the total flux linkage of the outer stator j phase; Ψ_{jout1} is the EMN calculated result of dual-stator part; Ψ_{jout2} is the EMN calculated result of the single-stator part.

The comparison of calculation results of U-phase flux linkage and phase EMF of inner and outer stator windings are shown in Fig. 15. and Fig. 16. respectively.

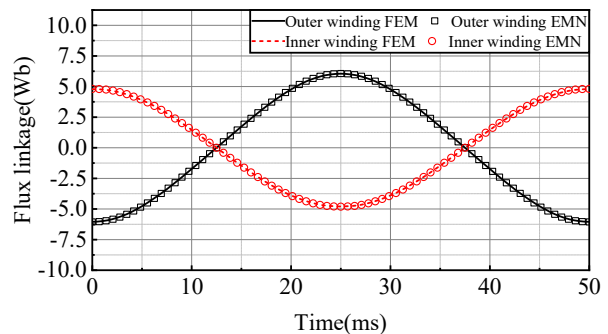


FIGURE 15. Comparison of no-load flux linkage

Because the saturation degree of stator teeth is low under no-load operation and the winding flux linkage is the sum of flux data of multiple teeth, the EMN results are highly consistent with the 3D FEM results. The EMN results of the

flux linkage amplitude of the inner and outer stator windings are 4.81Wb and 6.05Wb respectively.

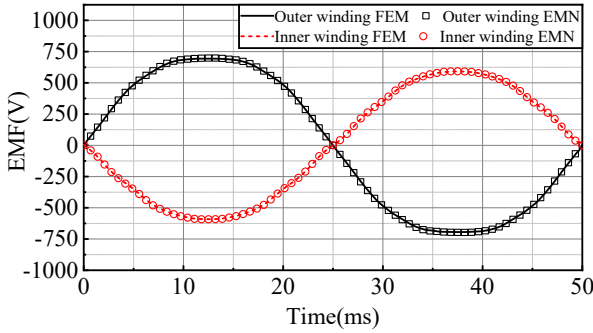


FIGURE 16. Comparison of no-load EMF

Since the EMF is related to the derivative of the flux linkage with respect to time, a highly consistent flux linkage results in the same highly consistent EMF results. The EMN and FEM results of the EMF effective value of the inner stator winding are 428.4V and 426.8V, respectively. The results of the outer stator winding are 531.6V and 528.6V respectively.

It is worth noting that the maximum input current and limit output torque of the surface-mounted motor under $i_d=0$ control are shown in (18) and (19), in order to ensure that the inner stator outputs the required torque within the voltage limit, so the number of turns and EMF effective value are designed to be low[24].

$$i_{s\max} = \frac{\sqrt{v_{\lim}^2 (R_s^2 + X_s^2) - X_s^2 e_0^2} - e_0 R_s}{R_s^2 + X_s^2} \quad (18)$$

$$T_{em\lim} = \frac{3}{2\omega_m} \frac{e_0 \sqrt{v_{\lim}^2 (R_s^2 + X_s^2) - X_s^2 e_0^2} - e_0^2 R_s}{R_s^2 + X_s^2} \quad (19)$$

where, v_{\lim} is the limiting terminal voltage of the motor; R_s is the winding phase resistance; X_s is the synchronous reactance; e_0 is the no-load EMF.

B. PERFORMANCE COMPARISON UNDER NO-BOOST OPERATION

When the IBPMM is running under no-boost operation, the current of the inner stator winding is zero, and only the outer stator winding is fed with current to generate torque. When 59A rated current is passed into the outer stator, the radial air-gap flux density and flux linkage of the IBPMM are shown in Fig. 17. and Fig. 18. respectively. Because the current is small, the saturation degree of the common rotor yoke changes little, therefore, the radial air-gap flux density and flux linkage of the inner stator are consistent with that of the no-load operation. The EMN results of the outer stator air-gap flux density are in good agreement with the FEM results, and the errors of the dual-stator and the single-stator parts are 2.8% and 3.1%, respectively.

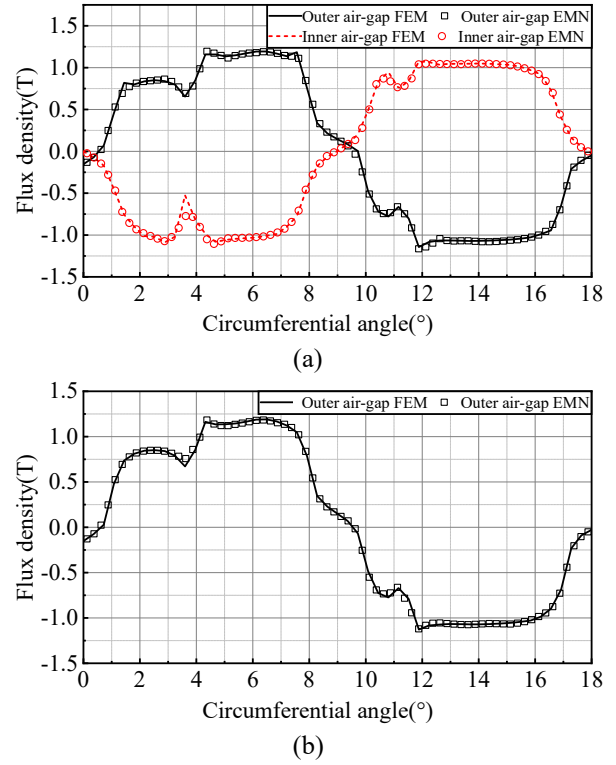


FIGURE 17. Comparison of air-gap radial flux density under no-boost operation (a) Dual-stator part (b) Single-stator part

The current of the outer stator winding increases the saturation degree of the core, resulting in a larger slot flux leakage error between the EMN model and the FEM. As a result, the EMN calculation results of the outer stator flux linkage are slightly higher than the FEM results, and their amplitudes are 6.39Wb and 6.31Wb respectively.

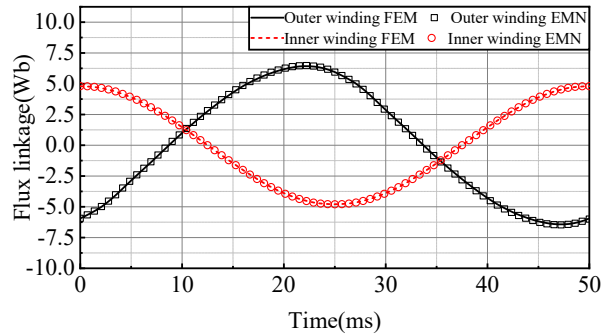


FIGURE 18. Comparison of flux linkage under no-boost operation

After calculating the load flux linkage, the average electromagnetic torque of the motor can be obtained according to (20) [24]:

$$T_{em} = \frac{3}{2} p (\Psi_d i_q - \Psi_q i_d) \quad (20)$$

where, p is the number of pole pairs; The q- and d-axis flux linkage Ψ_q , Ψ_d and the q and d axis current i_q , i_d can be obtained by the coordinate transformation of (21) - (23):

$$\begin{bmatrix} \Psi_d \\ \Psi_q \end{bmatrix} = \mathbf{C} \begin{bmatrix} \Psi_U \\ \Psi_V \\ \Psi_W \end{bmatrix} \quad (21)$$

$$\begin{bmatrix} i_d \\ i_q \end{bmatrix} = \mathbf{C} \begin{bmatrix} i_U \\ i_V \\ i_W \end{bmatrix} \quad (22)$$

$$\mathbf{C} = \frac{2}{3} \begin{bmatrix} \cos \theta & \cos\left(\theta - \frac{2}{3}\pi\right) & \cos\left(\theta + \frac{2}{3}\pi\right) \\ -\sin \theta & -\sin\left(\theta - \frac{2}{3}\pi\right) & -\sin\left(\theta + \frac{2}{3}\pi\right) \end{bmatrix} \quad (23)$$

The total electromagnetic torque T_{em} of the IBPMM is the sum of the electromagnetic torque of the inner and outer stators [25]:

$$T_{em} = T_{em1} + T_{em2} \quad (24)$$

where, T_{em1} is the electromagnetic torque generated by the outer stator; T_{em2} is the electromagnetic torque generated by the inner stator. When the IBPMM is running under the no-boost operation, $T_{em2}=0$.

The variation trend of the average electromagnetic torque of the motor at different outer stator currents is shown in Fig. 19. The additional electromagnetic torque provided by the unequal-length outer stator core part is 30% of that provided by the equal-length part. With the increase of the current, the saturation degree of the outer stator increased, and the error between the EMN result and the FEM results become larger. The result of EMN calculation at the maximum current is 1.2% higher than that of FEM.

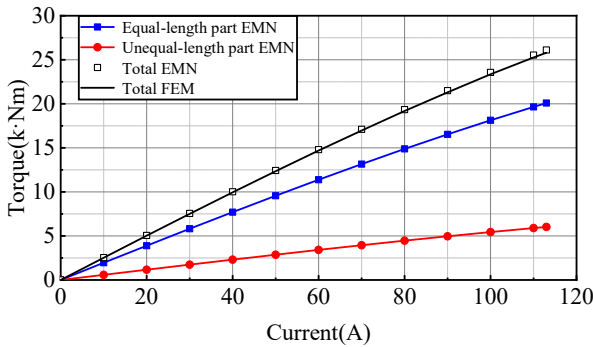


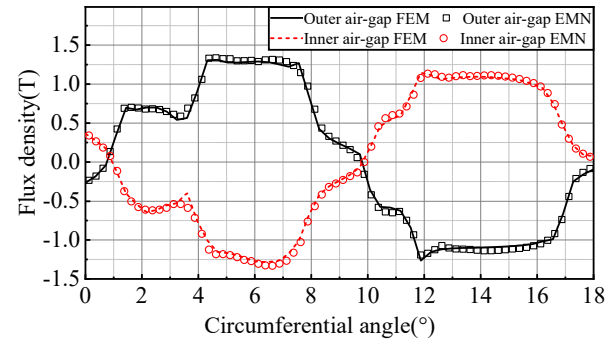
FIGURE 19. Comparison of torque under no-boost operation

C. PERFORMANCE COMPARISON UNDER INNER BOOST OPERATION

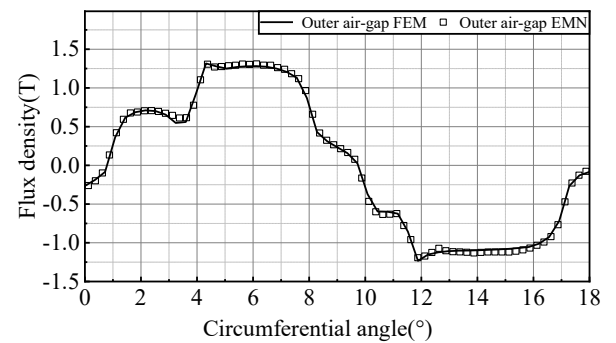
When the IBPMM is running under inner boost operation, both the inner and outer stator windings are fed with current to generate torque, but the current of the outer stator windings remains unchanged at 105A. The air-gap flux density and flux linkage of the IBPMM under maximum inner boost operation are shown in Fig. 20. and Fig. 21.

Due to the higher degree of saturation, the errors between the EMN results and the FEM results of the inner stator are larger than that of the outer stator. The inner and outer air-

gap flux density errors of the dual-stator part are 4.9% and 3.8%, respectively, and the error of single-stator part is 3.6%. The EMN and FEM results of the outer stator flux linkage amplitudes are 7.0Wb and 6.88Wb, respectively, and the inner stator flux linkage amplitudes are 6.12Wb and 5.94Wb.



(a)



(b)

FIGURE 20. Comparison of air-gap radial flux density under inner boost operation (a) Dual-stator part (b) Single-stator part

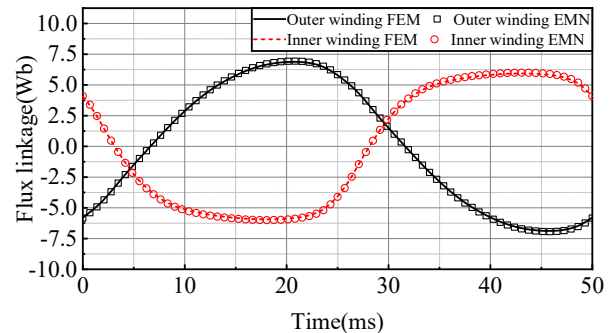


FIGURE 21. Comparison of flux linkage under inner boost operation

Under the premise of satisfying the mechanical strength, a thinner rotor yoke can improve the torque density of the inner stator. However, because the saturation flux density of the rotor yoke material is low and the saturation degree is greatly affected by the large inner stator current, too thin rotor yoke will cause the output torque of the outer stator to decrease due to saturation. The rotor yoke flux density distribution of the prototype is shown in Fig. 22. under no-boost and maximum inner boost operations, the maximum flux density

of the rotor yoke center under the two operations are 1.42 T and 1.61T, respectively.

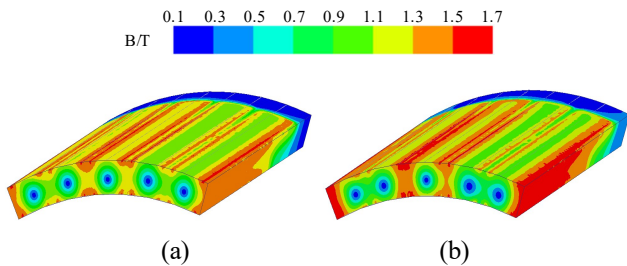


FIGURE 22. Flux density distribution of rotor yoke under different boost currents (a) No-boost current (b) Maximum inner boost current

The output torque generated by the inner stator and the outer stator can be separated using the proposed EMN model. The output torque of the IBPMM at different inner boost currents is shown in Fig. 23. With the increase of the inner boost current, the saturation degree of the inner stator core increases, resulting in a nonlinear increase in the output torque of the inner stator, and the error between the EMN result and the FEM result becomes larger. The EMN result of the total electromagnetic torque at the maximum inner boost current is 2.1% higher than the FEM result. In addition, when the current of the inner stator reaches 110A, the flux density of the rotor yoke enters the nonlinear range, resulting in a slight decrease in the output torque of the outer stator. Compared to the no-boost operation, the output torque of the outer stator decreased by approximately 0.5% when the maximum inner boost current is applied. The FEM is difficult to separate the torque, so it is useful to use the proposed EMN model to optimize the rotor yoke thickness.

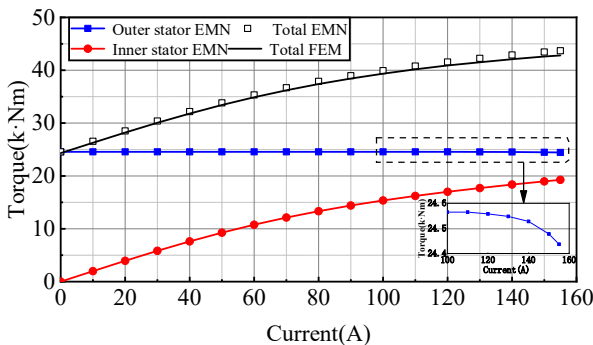


FIGURE 23. Comparison of torque under boost operation

D. COMPARISON OF COMPUTING EFFICIENCY

Table II shows the number of computing elements, computing time and memory consumption by quasi-3D EMN and 3D FEM when solving one electrical cycle for the 1/8 model IBPMM. From the comparison results, it can be seen that the quasi-3D EMN method can obtain satisfactory calculation accuracy through fewer elements, greatly reduce the computing time, and reduce the requirements of the computer hardware.

TABLE II

Comparison of computational efficiency

Parameter	Quasi-3D EMN	3D FEM
Number of computing elements	1294	2252573
Computing time	0.4h	11.9h
Consume memory	1.2GB	67.3GB

V. PROTOTYPE EXPERIMENT

The experimental platform of IBPMM prototype is shown in Fig. 24.

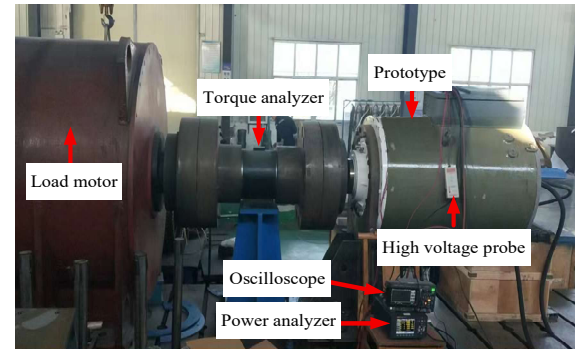


FIGURE 24. Prototype experimental platform

The prototype is dragged to the rated speed by the test machine, the comparison between the measured EMF and the calculated results of EMN are shown in Fig. 25.

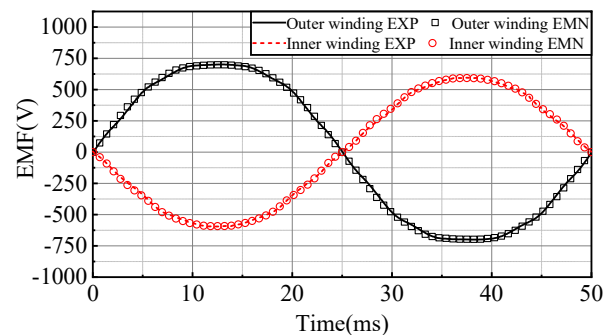


FIGURE 25. Experimental results of no-load EMF

The experimental results are highly consistent with that of the quasi-3D EMN model, however, owing to the cutting angle of PMs, the experimental waveforms and values are slightly different from the EMN results. The effective values of the EMN experimental results of the inner and outer stator windings are 424.6V and 526.9V respectively.

During the loading experiment, because the rotor adopts the surface-mounted structure, the $i_d=0$ control is adopted for both the inner and outer stators. The output torque of the IBPMM at different currents are obtained by gradually increasing the power of the test machine. The comparison between experimental results and EMN calculation results are shown in Fig. 26.

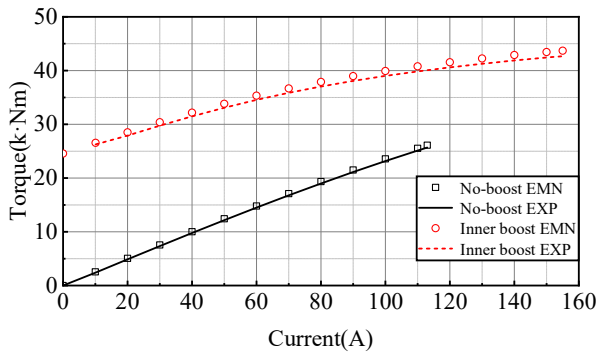


FIGURE 26. Comparison of FEM and measured results

When the IBPMM is under inner boost operation, with the increase of the current of the inner stator winding, the error between the two results gradually becomes larger, this is because the saturation degree of the inner stator core increases with the increase of the current of the inner stator winding, which affects the calculation accuracy of EMN model, at the same time, the output torque of the experimental motor decreases with the increase of iron loss and PMs temperature. When the inner motor is running at the maximum current, the EMN result is 3.2% higher than the experimental result, this error is within the acceptable range of engineering.

VI. CONCLUSION

In order to improve the space utilization rate and short-term overload capacity of the DSPMM, an IBPMM with unequal-length cores is proposed in this paper. Aiming at the characteristic of the IBPMM with different sections along the axis, a quasi-3D EMN model is established to separate the inner stator torque and outer stator torque, and further analyze the influence of the large inner stator current on the outer stator torque, which provides a basis for the optimization of the rotor yoke thickness. Meanwhile, the computing efficiency is improved. Through the analysis, research of the quasi-3D EMN model and prototype experiments, the following conclusions can be obtained:

- 1) The unequal-length cores structure of the IBPMM can make full use of the inner space of the motor to increase the output torque of the outer stator by 30%. At the same time, the short-term boost running inner stator can make the IBPMM reach 3 times short-time overload under the $i_d=0$ control.
- 2) The high current density of the inner stator winding will increase the saturation of the rotor yoke and thus affects the output torque of the outer stator. The output torque of the outer stator at the maximum inner boost current is only 0.5% lower than that of the no-boost operation under the condition of the rotor yoke thickness of the prototype.
- 3) The results of the proposed quasi-3D EMN are in good agreement with those of the 3D FEM under no-load operation. The torque calculation results of the quasi-3D EMN are 1.2% and 2.1% higher than those

of 3D FEM under no-boost and maximum inner boost operations, respectively. In addition, the solving time of the quasi-3D EMN model is only 3.4% of that of the 3D FEM, which significantly improves the solving speed of IBPMM and reduces the requirements for computer configuration.

- 4) The torque results of the quasi-3D EMN are 1.8% and 3.2% higher than the experimental results under no-boost and maximum inner boost operations, respectively, the errors meet the engineering requirements. The performance of the IBPMM and the accuracy of the quasi-3D EMN model can be proved.

REFERENCES

- [1] Y. He, Y. Tang, X. Gao, *et al.*, "Direct predictive voltage control for grid-connected permanent magnet synchronous generator system," *IEEE Transactions on Industrial Electronics*, vol. 70, no. 11, pp. 10860-10870, 2023.
- [2] E. Lu, W. Li, X. Yang, *et al.*, "Composite sliding mode control of a permanent magnet direct-driven system for a mining scraper conveyor," *IEEE Access*, vol. 5, pp. 22399-22408, 2017.
- [3] B. Gan, B. Zhang, G. Feng, *et al.*, "Design and Analysis of Modular Permanent Magnet Fault-Tolerant Motor for Ship Direct-Drive Propulsion," *IEEE Transactions on Electrical and Electronic Engineering*, vol. 16, no. 9, pp. 1260-1278, 2021.
- [4] L. Fang, D. Li, X. Ren, *et al.*, "A novel permanent magnet vernier machine with coding-shaped tooth," *IEEE Transactions on Industrial Electronics*, vol. 69, no. 6, pp. 6058-6068, 2022.
- [5] R. Koster, A. Binder, "Multi-objective optimization of a direct-drive wind turbine generator with HTS excitation winding," *IEEE Transactions on Applied Superconductivity*, vol. 32, no. 4, pp. 1-8, 2022.
- [6] Z. Zhang, S. Yu, F. Zhang, *et al.*, "Electromagnetic and structural design of a novel low-speed high-torque motor with dual-stator and PM-reluctance rotor," *IEEE Transactions on Applied Superconductivity*, vol. 30, no. 4, pp. 1-5, 2020.
- [7] S. Jin, H. Wang, S. Yu, *et al.*, "Maximum torque per ampere control of permanent magnet/reluctance hybrid rotor dual stator synchronous motor," *IET Electric Power Applications*, vol. 18, no. 9, pp. 1021-1032, 2024.
- [8] J. Zhang, B. Zhang, G. Feng, *et al.*, "Design and analysis of a low-speed and high-torque dual-stator permanent magnet motor with internal enhanced torque," *IEEE Access*, vol. 8, pp. 182984-182995, 2020.
- [9] D. Li, R. Qu, W. Xu, *et al.*, "Design procedure of dual-stator spoke-array vernier permanent-magnet machines," *IEEE Transactions on Industry Applications*, vol. 51, no. 4, pp. 2972-2983, 2015.
- [10] S. Asgari, M. Mirsalin, "A novel dual-stator radial-flux machine with diametrically magnetized cylindrical permanent magnets," *IEEE Transactions on Industrial Electronics*, vol. 66, no. 5, pp. 3605-3614, 2019.
- [11] J. Song, J. Lee, D. Kim, *et al.*, "Analysis and modeling of concentrated winding variable flux memory motor using magnetic equivalent circuit method," *IEEE Transactions on Industry Electronics*, vol. 53, no. 6, pp. 1-4, 2017.
- [12] Y. Liu, Z. Zhang, J. Ji, *et al.*, "Electromagnetic performance analysis of a new hybrid excitation synchronous machine for electric vehicle applications," *IEEE Transactions on Magnetics*, vol. 54, no. 11, pp. 1-4, 2018.
- [13] D. Cao, W. Zhao, C. Wang, *et al.*, "Parametric equivalent magnetic network modeling approach for multiobjective optimization of PM machine," *IEEE Transactions on Industrial Electronics*, vol. 68, no. 8, pp. 6619-6629, 2021.
- [14] M. Ghods, H. Gorginpour, J. Faiz, *et al.*, "Design and enhanced equivalent magnetic network modeling of a fractional-slot spoke-array vernier PM machine with rotor flux barriers," *IEEE*

- Transactions on Energy Conversion*, vol. 38, no. 2, pp. 1060-1072, 2023.
- [15] W. Tong, Y. Yao, S. Li, *et al.*, "Equivalent magnetic network model for interior permanent magnet machines considering non-uniform saturation of magnetic bridges," *Transactions of China Electrotechnical Society*, vol. 37, no. 12, pp. 2961-2970, 2022.
- [16] C. Zhang, Z. Chen, Q. Mei, *et al.*, "Nonlinear dynamic equivalent magnetic network model analysis of transverse flux permanent magnet synchronous motor," *Proceedings of the CSEE*, vol. 39, no. 1, pp. 307-314+345, 2019.
- [17] M. Ghods, H. Gorginpour, M. Bazrafshan, *et al.*, "Equivalent magnetic network modeling of dual-winding outer-rotor vernier permanent magnet machine considering pentagonal meshing in the air-gap," *IEEE Transactions on Industrial Electronics*, vol. 69, no. 12, pp. 12587-12599, 2022.
- [18] G. Liu, S. Jiang, W. Zhao, *et al.*, "Modular reluctance network simulation of a linear permanent-magnet vernier machine using new mesh generation methods," *IEEE Transactions on Industrial Electronics*, vol. 64, no. 7, pp. 5323-5332, 2017.
- [19] H. Ke, Z. Liu, Q. Chen, *et al.*, "Analysis of a spoke-type ferrite PM motor with assisted poles based on equivalent magnetic network with hybrid cross-shaped mesh elements," *IET Electric Power Applications*, vol. 17, no. 4, pp. 474-486, 2023.
- [20] J. Hou, W. Geng, Q. Li, *et al.*, "3-D equivalent magnetic network modeling and FEA verification of a novel axial-flux hybrid-excitation in-wheel motor," *IEEE Transactions on Magnetics*, vol. 57, no. 7, pp. 1-12, 2021.
- [21] J. Bai, G. Liu, J. Lang, *et al.*, "Equivalent magnetic network model for dual-winding dual-flux-concentrated magnetic-field-modulated brushless compound-structure machine," *IEEE Transactions on Energy Conversion*, vol. 39, no. 2, pp. 1446-1455, 2024.
- [22] G. Liu, Y. Wang, Q. Chen, *et al.*, "Design and analysis of a new equivalent magnetic network model for IPM machines," *IEEE Transactions on Magnetics*, vol. 56, no. 6, pp. 1-12, 2020.
- [23] W. Tong, P. Wang, S. Wu, *et al.*, "Electromagnetic performance analysis of a hybrid excitation synchronous machine based on 3D equivalent magnetic network," *Transactions of China Electrotechnical Society*, vol. 38, no. 3, pp. 692-702, 2023.
- [24] J. Wu, G. Feng, Y. Hu, *et al.*, "Analysis of limiting output capacity of low-speed and high-torque surface-mounted permanent magnet motor considering resistance voltage drop," *IEEE Access*, vol. 11, pp. 88059-88073, 2023.
- [25] J. Wu, Y. Hu, B. Zhang, *et al.*, "Comparison and analysis of different rotor structure of double-stator permanent magnet synchronous motor," *IET Electric Power Applications*, vol. 17, no. 4, pp. 421-431, 2022.



Jiacheng Wu received the B.S. degree in electrical engineering and automation from Shenyang University of Technology, Shenyang, China, in 2015 and received the Master degree in electrical engineering and automation from Shenyang University of Technology, Shenyang, China, in 2020. He is currently pursuing the Ph.D. degree in electrical engineering from Shenyang University of Technology, Shenyang, China. His research interests include design and control of permanent magnet motor.



Shuai Wang received the B.S. degree in Computer Science and Technology from Liaoning Technical University, Fuxin, China, in 2004, received the M.S. and Ph.D. degrees in electrical engineering from Shenyang University of Technology, Shenyang, China, in 2007 and 2016. He is currently a lecturers with electrical engineering from Shenyang University of Technology, Shenyang, China. His research

interests include design and optimization of electrical machines and low speed high torque drive system.



Yan Hu received the Ph.D. in electrical engineering from Shenyang University of technology. Her research field is special motor and its control and numerical analysis of the electromagnetic field.

From 2004 to 2020, she is the director of Electrical Engineering Department of Shenyang University of Technology and director of Institute of motion control motor. Executive director of the electromagnetic field teaching and Teaching Materials Research Association of Chinese colleges and universities.



Bingyi Zhang received the Ph.D. in electrical engineering from Shenyang University of technology, is Member of China Electrical Engineering Society and IEEE-IAS. He is Senior electrical bid evaluation expert of China International Tendering Corporation. His research field is Motor and its control.



Xuefeng Xu received the B.S., M.S. and Ph.D. degrees in electrical engineering from Shenyang University of Technology, Shenyang, China, in 2003, 2009, and 2024 respectively. His major research interests include the design, analysis and control of permanent magnet machines for electric vehicle, and low-speed direct-drive permanent magnet machines.